RSC Advances

PAPER

View Article Online
View Journal | View Issue

Cite this: *RSC Adv.*, 2026, **16**, 8798

Self-assembled monolithic β-FeOOH/copper foam catalysts for enhanced catalytic reduction of nitrogen-containing contaminants in continuous-flow systems

Shan Tai,[a] Yan Wu,[a] Renliang Wang,*[b] Kun Liu *[b] and Guofeng Zhao*[a]

Due to its relatively automated and straightforward operational process, continuous-flow catalysis has emerged as a promising technology for treating nitrogen-containing contaminants. However, achieving high activity and low flow resistance in packed-bed catalysts within continuous-flow systems remains a grand challenge. This study successfully constructed an integrated catalyst with a three-dimensional multi-level pore structure by self-assembling nano-flower-like β-FeOOH active components on a copper foam substrate. This catalyst can be easily integrated into a fixed-bed platform to build an efficient and stable continuous-flow catalytic system. The catalyst exhibited exceptional performance, achieving complete reduction of 4-nitrophenol within 49 s and maintaining over 98.2% catalytic efficiency after 10 consecutive cycles. It also demonstrated broad-spectrum activity, degrading various organic dyes such as methylene blue, Congo red, Rhodamine B, and methyl orange within 121 s. The substantial enhancement of catalytic activity is primarily attributed to the synergistic effects of three key factors: (1) efficient mass transfer enabled by the 3D hierarchical pore structure of the nano-flower-like β-FeOOH; (2) fully exposed active sites – Fe^{3+} on β-FeOOH catalyzes the hydrolysis of BH_4^- to generate active hydrogen species (H*); and (3) the sustainable Fe^{3+}/Fe^{2+} redox cycle maintained by CF's excellent electron conductivity: CF transfers electrons to Fe^{2+} (generated from Fe^{3+} reduction during H* production) to regenerate Fe^{3+}, ensuring continuous catalytic kinetics. This enhancement mechanism provides a new strategy for designing high-performance environmental catalytic materials. By integrating multiphase catalysis with flow chemistry technology, this study not only expands the conceptual framework for constructing environmental catalytic materials but also offers a more scalable, efficient, and environmentally compatible solution for wastewater treatment.

Received 5th December 2025
Accepted 1st February 2026

DOI: 10.1039/d5ra09414c

rsc.li/rsc-advances

1. Introduction

With the increase in the production and consumption of fine chemicals, large amounts of pollutants are discharged into the natural environment, leading to severe water pollution. Nitrogen-containing contaminants commonly found in industrial and agricultural wastewater are difficult for microorganisms in the natural environment to degrade rapidly due to their complex aromatic ring structures. They exhibit persistence, biotoxicity, and bioaccumulation, posing potential threats to humans, plants, and aquatic organisms.[1–9] Currently, various methods exist for treating nitrogen-containing contaminants, including physical adsorption,[10,11] catalytic reduction,[12,13] membrane separation,[14,15] electrochemical processes[16,17] and microbial degradation.[18,19] Among these, catalytic reduction demonstrates significant advantages in sustainability, cost-effectiveness, and treatment efficiency, making it a promising wastewater treatment technology for nitrogen-containing contaminants.[20] This technology can reduce nitroaromatics and azo dyes to less toxic amino aromatics, which themselves are high-value-added chemical products.[21,22] Consequently, the development of novel nanocatalysts with high catalytic activity for the reduction reaction of nitrogen-containing contaminants has attracted widespread interest among researchers.

Continuous-flow catalytic reduction represents a more efficient, safer, precise, and environmentally friendly modern chemical production process compared to traditional batch reactions, offering significant advantages in chemical, pharmaceutical, and fine chemical manufacturing.[23,24] As a representative flow chemistry system, fixed beds enable maximization of catalytic reaction throughput at high rates. As a vital component of fixed-bed systems, packed catalysts play an indispensable role in

[a]*Key Laboratory of Functional Molecular Solids Ministry of Education, College of Chemistry and Materials Science, Anhui Normal University, Wuhu 241002, China. E-mail: gfzhao@ahnu.edu.cn*

[b]*Institute of Optical Functional Materials for Biomedical Imaging, School of Chemistry and Pharmaceutical Engineering, Shandong First Medical University & Shandong Academy of Medical Sciences, Taian 271016, China. E-mail: renliangw@163.com; liukun2436@126.com*

continuous catalytic processes.[25] Most currently reported catalysts exist in granular or powdered forms, and these traditional heterogeneous catalytic systems suffer from inherent limitations. First, the separation, purification, and recovery of catalysts from aqueous suspensions involve complex processes. Second, catalyst agglomeration reduces active site exposure and increases flow resistance, severely limiting their practical application. Monolithic catalysts often hold greater industrial value than powdered catalysts due to advantages such as lower pressure drop, uniform heat transfer, and structural stability.[26] Foam metals were widely recognized as excellent supports due to their exceptional heat transfer rates and pore structures.[27] For instance, Pan *et al.* successfully prepared an integrated MnO_2–O_v/CF catalyst with abundant oxygen vacancies by inducing *in situ* MnO_2 growth on foam copper *via* a redox method. This catalyst effectively promotes the combustion reaction of toluene.[28] Katerina Soulantica *et al.* employed hcp-Co nanowires grown on metal foam as catalysts for Fischer–Tropsch synthesis.[29] Additionally, Dang *et al.* developed an integrated catalyst by loading ZIF-derived Co_3O_4 onto foam copper for toluene catalytic oxidation.[30] Thus, preparing monolithic catalysts by *in situ* growth of nanomaterials on metallic foams represents a promising strategy, poised to become a significant development direction for chemical process intensification and green manufacturing.

Iron-based nanomaterials, as abundant, low-cost, and environmentally friendly materials, including iron sulfide (FeS), iron oxides (Fe_2O_3, Fe_3O_4), hydroxy iron oxides (FeOOH) and their derivatives, serve as ideal materials for efficiently treating toxic nitrogen-containing contaminants due to their high efficiency and reactivity.[31–33] Among these, tetragonal goethite (β-FeOOH), an easily accessible hydroxyl iron oxide derived from iron-based precursors, demonstrates significant application potential in the afore mentioned catalytic reactions. Its abundant surface hydroxyl functional groups not only promote the adsorption and activation of reducing agents but also confer excellent hydrophilicity and dispersibility to the material. More importantly, its inherent multivalent iron centers effectively facilitate electron transfer, driving the hydrogenation reduction of nitro or chromophore groups.[34,35] However, nanoscale β-FeOOH particles are prone to agglomeration, limiting their applications. Consequently, current research focuses on overcoming these limitations through strategies such as morphology control, elemental doping, or heterojunction construction. Copper exhibits high activity and selectivity toward nitro hydrogenation reactions while serving as an excellent electronic conductor.[36] When combined with β-FeOOH, this structure not only suppresses material agglomeration but also significantly enhances electron separation and transport, yielding synergistic catalytic effects.[37,38] This approach markedly improves the overall degradation efficiency and rate of nitrogen-containing pollutants, fully unlocking its application potential in advanced wastewater treatment.

Although previous studies have reported iron-based catalysts supported on foam metals for the reduction of nitroaromatics, most work has focused on batch reaction systems or simple particle-supported structures. In this study, we propose a controlled self-assembly hydrothermal strategy to construct an integrated nano-flower-like β-FeOOH@CF catalyst with a three-dimensional multi-level porous structure. This approach enables efficient catalytic reduction of various nitrogen-containing pollutants in a continuous-flow reactor. By self-assembling the β-FeOOH active component onto a porous copper foam (CF) substrate, we successfully constructed a catalyst system featuring a three-dimensional multi-level pore structure. This structure facilitates direct loading into glass columns, forming a catalytic unit suitable for continuous-flow reactors such as fixed beds. Benefiting from abundant mass transfer pathways and fully exposed active sites, the constructed fixed-bed system exhibits outstanding catalytic activity (complete reduction of 4-nitrophenol within 49 s) and long-term stability during the reduction of 4-nitrophenol. Furthermore, the catalyst demonstrates broad-spectrum degradation activity toward various organic dyes, maintaining over 98.2% catalytic performance after 10 consecutive cycles. These results demonstrate that β-FeOOH@CF represents a structurally stable, environmentally friendly, and easily scalable catalytic platform with broad application prospects for the efficient removal of harmful nitrogen-containing contaminants.

2. Experimental

2.1. Materials and characterization

The detailed materials, catalysts preparation, catalyst characterization and catalyst evaluation were exhibited in the SI.

2.2. Continuous-flow catalytic system

The continuous-flow experiment was conducted in a vacuum-driven fixed-bed reactor. A glass column (inner diameter: 3.5 cm; length: 30 cm) was packed with the monolithic β-FeOOH@CF catalyst, forming a catalyst bed layer with a height of 0.5 cm and a bed volume of approximately 4.8 cm^3. The reaction solution containing pollutants and $NaBH_4$ was continuously drawn through the catalyst bed by a vacuum pump, with the flow rate fixed at 25 mL min^{-1} by controlling the pump suction force. Based on this, the average residence time of the fluid within the bed was calculated to be approximately 11.5 seconds. The Reynolds number (Re) calculated from the operating parameters was 15.16, confirming laminar flow conditions (Re < 2000). Benefiting from the three-dimensional open-pore structure of the catalyst, the pressure drop during the reaction process was negligible, demonstrating excellent fluid permeability. Despite the laminar flow regime, the hierarchical pore architecture of the catalyst promotes local fluid mixing and enhances mass transfer efficiency, ensuring adequate contact between reactants and active sites. This avoided the mass transfer limitations that laminar flow may cause, enabling the reaction to proceed efficiently in the kinetically controlled zone.

2.3. Kinetic analysis and evaluation

To investigate the reaction kinetics and determine the activation energy (E_a), The kinetic tests were performed at various temperature. The concentration of the target pollutant 4-nitrophenol (30 mM, 20 mL) the influent was fixed. The reduction of 4-nitrophenol, the $NaBH_4$ dosage was uniformly set at 100 equivalents.

The reaction rate constant (k) at each temperature was calculated based on the conversion efficiency and the residence time. Subsequently, the apparent activation energy was derived by fitting the data to the Arrhenius equation using a plot of $\ln(k)$ *versus* $1/T$.

2.4. The stability and durability measurements

To evaluate the stability of the β-FeOOH@CF catalyst and the durability of its fixed-bed reactor, we repeatedly performed the reduction reaction of 4-nitrophenol (4-NP) under continuous flow conditions. 20 mL of a mixed reaction solution containing 4-NP (5.0 mmol L^{-1}) and $NaBH_4$ was continuously passed through the β-FeOOH@CF catalytic assembly housed in a tubular reactor, the effluent from each catalytic reaction was analyzed using UV-visible spectrophotometry. After each catalytic cycle, the packed β-FeOOH@CF catalyst was washed with approximately 20 mL of deionized water.

3. Results and discussion

3.1. Characterization of β-FeOOH@CF

A monolithic nanoflower catalyst was synthesized *via* a self-assembly hydrothermal method, as shown in Fig. 1(a). This approach is advantageous as it enables precise control over the morphology and composition of the resulting nanomaterials. The pH regulator urea slowly decomposes under hydrothermal conditions to produce OH^- ions, providing the required alkaline environment. Its slow-release characteristic enables nucleation and growth processes within the solution to occur under controlled conditions. Meanwhile, the structure-directing agent ammonium fluoride supplies F^- ions that etch the metal surface, promoting nucleation and facilitating the formation of ordered nanostructures.[39] Specifically, the self-assembly process generates complex hierarchical structures, ultimately yielding a nanoflower morphology (Fig. 1(e and g)), which is crucial for enhancing catalytic activity. β-FeOOH was grown using CF as a template, The appearance of CF is first visible in Fig. 1(c), where the pristine CF exhibits a typical reddish-brown colour. Following the hydrothermal reaction, the foam copper darkens and turns black (Fig. 1(f)). Additionally, the microscopic image of CF is shown in Fig. 1(b and d), where the skeletal framework of the foam structure is readily observable. The surface of this framework is remarkably smooth, devoid of any noticeable objects. The energy-dispersive X-ray spectroscopy (EDS) mapping results reveal that copper (Cu) exhibits relatively uniform dispersion. Within the nanoflower structure regions, iron (Fe) and oxygen (O) signals show high overlap and uniform codistribution, directly confirming that

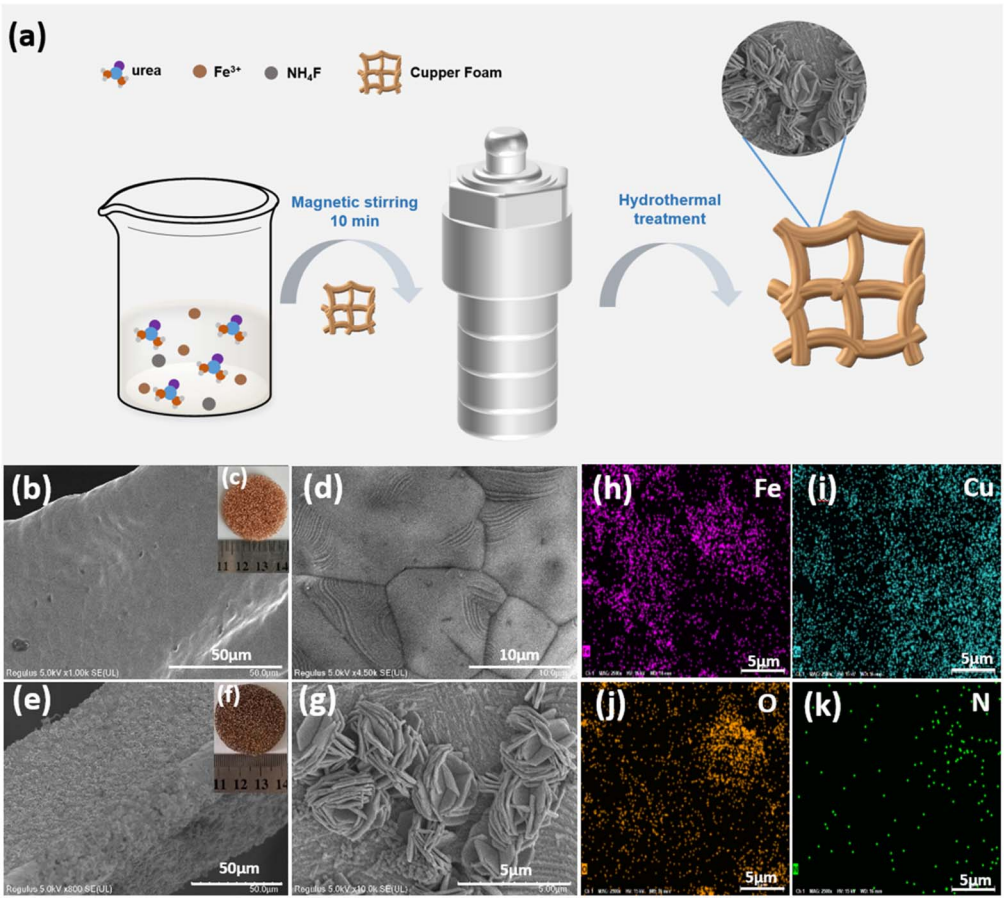

Fig. 1 (a) Schematic diagram illustrating the preparation procedure of the β-FeOOH@CF catalyst; (b and d) SEM images of commercial CF catalyst (inset in (c): optical photography of the pristine Cu-foam substrate); (e and g) SEM images of β-FeOOH@CF (12 h) catalyst (inset in (f): optical photography of the β-FeOOH@CF (12 h)); (h–k) element mapping diagram for β-FeOOH@CF (11 h).

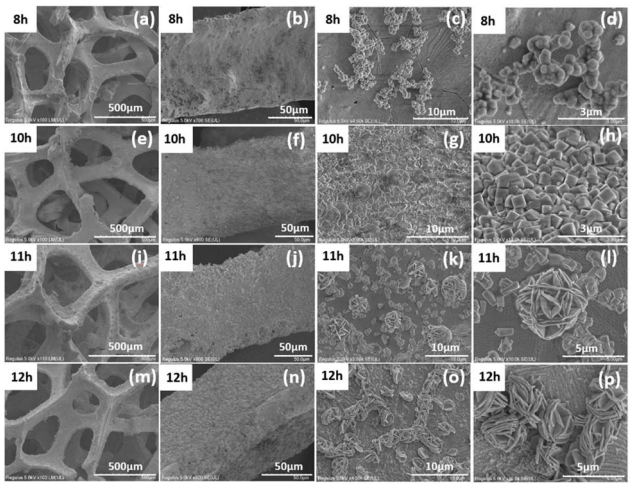

Fig. 2 SEM images and corresponding magnified morphologies of β-FeOOH@CF prepared at different hydrothermal reaction times: (a–d) 8 h; (e–h) 10 h; (i–l) 11 h; (m–p) 12 h.

the phase of this nanoflower structure is β-FeOOH (Fig. 1(h–k) and S1).

When iron species modify CF *via* the hydrothermal process, the sample primarily consists of well-dispersed, smooth-surfaced nanoparticles with an average diameter of approximately 500 nm after 8 hours of reaction time (Fig. 2(a–d)). Extending the reaction time to 10 hours triggered a significant morphological transformation: the original spherical nanoparticles evolved into two-dimensional nanosheets featuring distinct edges and smooth surfaces (Fig. 2(e–h)). Notably, further prolonging the reaction time to 11 hours led to increasingly complex structural evolution. The two-dimensional nanosheets undergo self-assembly, forming intricate three-dimensional hierarchical nanoflower structures (Fig. 2(i–l)). However, when the reaction time was prolonged to 12 hours, the CF framework was completely enveloped by the flower-like structure (Fig. 2(m–p)), which appeared to be an assembly of stacked and interpenetrating nanosheets with a thickness of 175 nm. These nanoflowers comprised numerous interconnected two-dimensional nanosheets, forming a highly porous architecture. This continuous evolution from spherical nanosheets to nanoflowers can be explained by the synergistic action of Ostwald ripening and directed attachment mechanisms.[40,41] Initially unstable spheres dissolve and recrystallize into thermodynamically stable nanosheet structures. Subsequently, these two-dimensional nanosheets self-assemble into intricate nanoflower architectures to minimize overall surface energy. This controllable morphological adjustment is crucial for regulating the material's specific surface area and catalytic performance. When the hydrothermal reaction time was extended to 14 hours, significant etching of the foam copper skeleton occurred (Fig. S2). To prevent excessive damage to the carrier structure, this study ultimately selected 12 hours as the optimal hydrothermal reaction duration.

The corresponding XRD pattern of the nanoflower-coated CF was shown in Fig. 3(a). Commercial foam copper exhibited three characteristic peaks at 43.3°, 50.4° and 74.1°, attributed to the (1 1 1), (2 0 0) and (2 2 0) crystal planes of copper (Fig. S3), respectively. The XRD pattern of this nanoflower-coated CF showed several sharp peaks at 11.9°, 16.9°, 26.9°, 34.4°, 35.3°, 39.3°, 46.6°, 52.3°, 56.2° and 64.7°, corresponding to the (110), (200), (130), (400), (211), (301), (411), (600), (251) and (541) crystal planes of β-FeOOH, confirming the β-FeOOH form of these nanoflower structures.[42,43] Two characteristic peaks at 35.4° and 38.7° were attributed to the (002) and (111) crystal planes of CuO, respectively; however, these peaks overlapped significantly with those of β-FeOOH and were not clearly discernible in the XRD pattern. Raman spectroscopy further confirmed the crystalline phase of the nanoflowers. Compared to commercial sponge copper, distinctive Raman peaks at 308 cm^{-1}, 405 cm^{-1}, 545 cm^{-1}, and 726 cm^{-1} (Fig. 3(b)) were assigned to the phase of β-FeOOH.[44] As shown in Fig. S4, the nitrogen adsorption–desorption isotherm indicated that compared to spherical catalysts (specific surface area of 1.17 m^2 g^{-1}), the specific surface area of nano-flower catalysts increased to 23.25 m^2 g^{-1}, demonstrating superior surface structural advantages. This result indicated that the unique cascading structure of the nano-flower catalyst significantly increased surface exposure, effectively resolving the issue of active site shielding caused by particle agglomeration in sph-erical structures. This provided more abundant active site accommodation space for catalytic reactions. More importantly, it created open mass transfer pathways, which were expected to significantly reduce mass transfer resistance in subsequent continuous-flow catalytic processes.

X-ray photoelectron spectroscopy measurements were then conducted to investigate the chemical states of various bound elements within the β-FeOOH@CF nanocomposite. Low-resolution spectra of the β-FeOOH@CF revealed the coexistence of Fe, O, C and Cu elements (Fig. S5), with binding

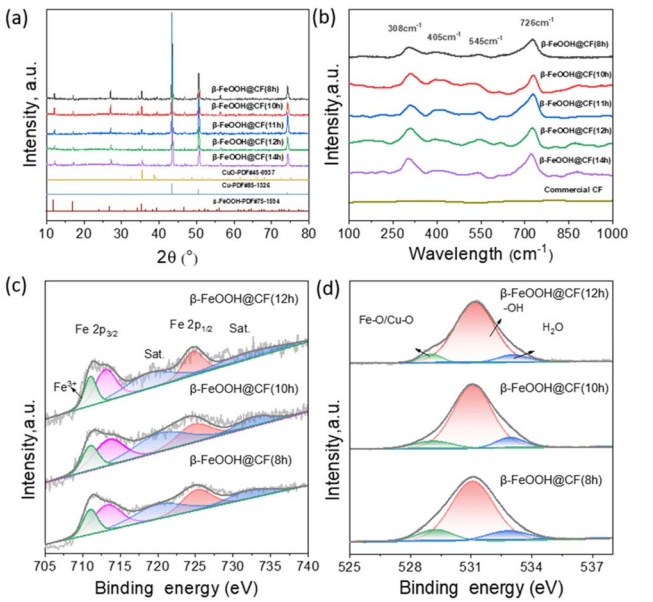

Fig. 3 (a) XRD patterns and (b) Raman spectra of the β-FeOOH@CF catalysts. (c and d) Fe 2p and O 1s XPS spectra for β-FeOOH@CF catalysts.

energies of approximately 711.0 eV, 532.0 eV, 284.8 eV and 932.6 eV corresponding to Fe 2p, O 1s, C 1s and Cu 2p signals.[45] The high-resolution XPS spectrum of the Fe 2p region presented in Fig. 3(c) displayed the corresponding spectra of samples prepared under different hydrothermal durations. All samples exhibited the characteristic spin–orbit doublet of Fe $2p_{3/2}$ and Fe $2p_{1/2}$. The main Fe $2p_{3/2}$ peak could be deconvoluted into two primary components. The dominant component located at a binding energy of approximately 711.05 eV was assigned to Fe^{3+} in the O═Fe(III)–OH structure within β-FeOOH crystals. The companion peak at 713.04 eV on the high-binding-energy side represented a multi-split secondary signal of Fe^{3+}.[46] A distinct shake-up satellite peak was observed at approximately 719.48 eV, which was a fingerprint for Fe^{3+} in octahedral coordination within an oxygen-dominated lattice. The consistent spectral characteristics above indicated that Fe^{3+} remained stable throughout the material under varying hydrothermal conditions, with β-FeOOH as the predominant phase. This confirmed that hydrothermal duration did not alter the chemical state or crystalline phase of iron.

The high-resolution O 1s spectrum, shown in Fig. 3(d), was asymmetric and could be fitted with three components, reflecting the complex chemical environment of oxygen in the sample. The peak at the lowest binding energy, typically around 529.03 eV, was assigned to lattice oxygen (O^{2-}) in the Fe–O bond of the FeOOH crystal structure and trace Cu–O bonds in oxidized copper.[47] The most intense component, centered at approximately 531.18 eV, was characteristic of hydroxyl groups (OH^-), which were the defining species in oxyhydroxides like FeOOH. The high intensity of this peak validated the hydroxide-rich nature of the material. The third component at a higher binding energy of 533.09 eV was attributed to physically adsorbed water molecules (H_2O).[36] The high relative area of the OH^- component was a direct evidence for the successful synthesis of the hydroxy-oxidized phase. Notably, as the hydrothermal time was extended from 8 h to 12 h, the relative content of surface OH^- ions increased significantly from 74% to 85%. This aligned with the evolution of the three-dimensional nanoflower structure observed *via* SEM-longer hydrothermal times promoted the formation of more developed nanoflowers with larger specific surface areas, thereby exposing more surface hydroxyl groups. This result further demonstrated that hydrothermal duration primarily regulated the assembly morphology of β-FeOOH without altering its crystalline phase. This phenomenon of "morphological evolution without phase change" could be attributed to the Ostwald ripening and oriented attachment mechanisms during growth, which influenced only the aggregation morphology of nanostructures without involving crystalline structural transformations. Fig. S6 displayed the high-resolution Cu 2p XPS spectrum of the β-FeOOH@CF(12 h) nanocomposite. The spectrum was characterized by the spin–orbit doublets of Cu $2p_{3/2}$ and Cu $2p_{1/2}$. The main Cu $2p_{3/2}$ peak could be deconvoluted into two distinct components. The dominant component at a binding energy of approximately 932.6 eV was indicative of Cu^0 (metallic copper). Crucially, the presence of a pronounced shake-up satellite peak at around 942.19 eV unambiguously confirmed the coexistence of Cu^{2+} species on the surface.[48] This suggested a partial oxidation of the copper foam substrate during the hydrothermal synthesis of β-FeOOH.

3.2. Catalytic performance evaluation of β-FeOOH@CF

Before investigating the catalytic activity of β-FeOOH@CF for reducing 4-NP, its adsorption capacity toward 4-NP was first evaluated. As shown in Fig. S7, the UV-vis spectrum of the 4-NP solution in the presence of β-FeOOH@CF exhibited no significant change over 10 minutes without $NaBH_4$, indicating that 4-NP cannot be removed by adsorption onto β-FeOOH@CF. Concurrently, Fig. 4(a) demonstrates that complete reduction of 4-NP can be achieved within 7.5 minutes using only commercial activated carbon and $NaBH_4$. Copper, as a common transition metal, can directly supply its surface electrons as a reducing agent to the 4-nitrophenol molecule, driving the conversion of the nitro group ($-NO_2$) to the amino group ($-NH_2$).[49]

In a continuous-flow reaction system, the catalytic reduction performance of β-FeOOH@CF as a catalyst was evaluated for several typical organic pollutants (Fig. 5(a) and S8), including 4-nitrophenol (4-NP), 3-nitrophenol (3-NP), 2-nitrophenol (2-NP), methyl orange (MO), Congo red (CR), Rhodamine B (RhB), and methylene blue (MB). All reactions were conducted under identical conditions: pollutant concentration of 5 mM, reaction volume of 20 mL, $NaBH_4$ as the reducing agent, and a fixed molar ratio of $NaBH_4$ to nitrogen-containing pollutants of 200 : 1. To validate the catalyst's universality and process characteristics, batch reaction control experiments were conducted in this study.

Under identical reaction conditions, both batch and continuous flow systems achieved complete removal of target pollutants within one minute. UV-visible spectroscopy monitoring revealed that the characteristic absorption peak of 4-NP at 397 nm

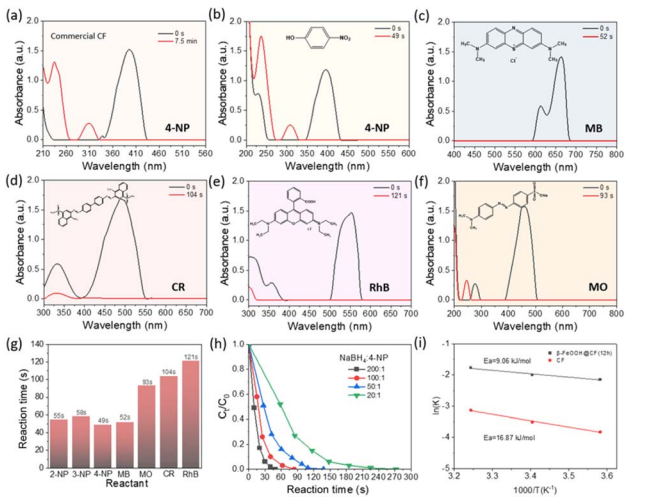

Fig. 4 (a) UV-vis spectra of commercial CF for the 4-NP reduction reaction; UV-vis spectra of β-FeOOH@CF (12 h) for the (b) 4-NP, (c) MB, (d) CR, (e) RhB (f) MO reduction reaction; (g) comparison of performance for seven pollutants: 2-NP, 3-NP, 4-NP, MB, MO, CR and RhB; (h) the effect of the ratio of $NaBH_4$:4-NP on the catalytic performance of β-FeOOH@CF (12 h); (i) the activation energy of β-FeOOH@CF (12 h) and CF in catalysing the reduction of 4-NP.

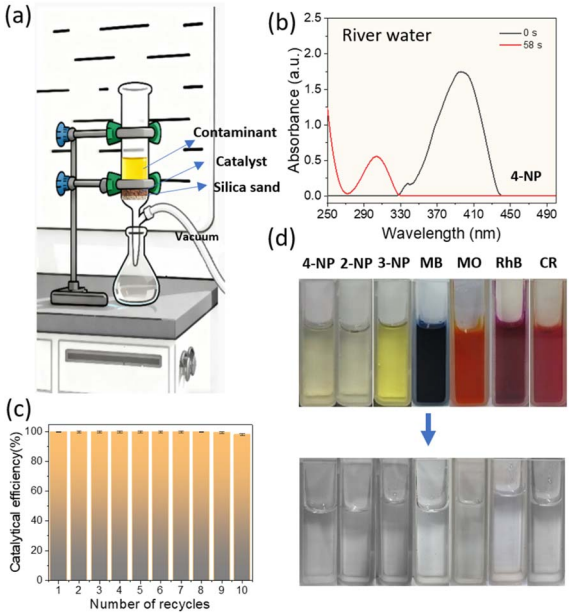

Fig. 5 (a) Schematic diagram showing the fixed-bed system constructed with the β-FeOOH@CF; (b) UV-vis spectra of 4-NP reduction in the river water; (c) the recycling catalytic performance of β-FeOOH@CF (12 h) for the reduction of 4-NP; (d) photographs of the seven aqueous solutions of organic dyes (4-NP, 3-NP, 2-NP, MO, CR, RhB and MB) and their corresponding reaction solution after continuous-flow reduction.

completely disappeared within 53 s in the batch reaction (Fig. S9). In contrast, after 49 s of flow reaction (SI video), the characteristic absorption peak of 4-NP at approximately 397 nm completely disappeared, while a new absorption band of 4-AP appeared at approximately 305 nm (Fig. 4(b)). Similar spectral shifts and decolorization phenomena were observed for other pollutants: 2-NP (55 s), 3-NP (58 s), MO (Fig. 4(f), 93 s), CR (Fig. 4(d), 104 s), RhB (Fig. 4(e), 121 s), and MB (Fig. 4(c), 52 s). The inset in Fig. 5(d) shows that the decolorization changes in the reaction solution further confirm the reduction of these dyes. The disappearance of RhB's characteristic peak at 552 nm confirms the destruction of its chromophore structure; the attenuation of MB's absorption peak at 663 nm reflects the cleavage of the thiazine parent nucleus; The disappearance of absorption peaks at 460 nm for MO and at 497 nm for CR directly demonstrates the breaking of azo bonds.[50–55] These spectral changes fully confirm that β-FeOOH@CF can effectively disrupt the characteristic chromophore structures of various pollutants, achieving highly efficient catalytic reduction (Fig. S10). Under the premise of fixed initial pollutant concentration and catalyst dosage, we progressively reduced the molar ratio of $NaBH_4$ to pollutant from 200 : 1 to 20 : 1 and investigated the pollutant removal efficiency. The supplementary experiments demonstrate that the β-FeOOH@CF catalyst prepared in this study still achieved a 100% pollutant removal rate within 272 seconds (Fig. 4(h)), even when the molar ratio of $NaBH_4$ to pollutant was significantly reduced from 200 : 1 to 20 : 1. This confirms that the catalyst remains capable of efficient pollutant removal under more economical and environmentally friendly conditions with low reductant dosage. Catalytic performance testing indicates that hydrothermal synthesis time significantly influences the morphology of foam copper-anchored β-FeOOH and its catalytic activity for the reduction of 4-nitrophenol. Specifically, the spherical structure formed after 8 hours of synthesis required 156 s to complete the reduction, whereas the nano-flower structure achieved the same in just 49 s, demonstrating superior catalytic efficiency. This advantage is primarily attributed to the nano-flower structure exposing a greater number of active sites (Fig. S11).

The kinetic testing (Fig. S12) demonstrated that the reaction was thermodynamically favorable for both catalysts at elevated temperatures, with an increase in the rate constant (k). To calculate the activation energy (E_a), the plots of $\ln(k)$ *vs.* $1/T$ (Fig. 4(i)) and the classical Arrhenius equation were utilized. The E_a values for β-FeOOH@CF and CF are 9.06 kJ mol^{-1} and 16.87 kJ mol^{-1}, respectively. Notably, the lower E_a of β-FeOOH@CF catalyst, compared to the pure copper foam, indicates higher catalytic activity and efficiency.[56,57] This suggests the catalytic reduction process is kinetically controlled. This characteristic, combined with the excellent mass transfer capability provided by its unique porous structure, collectively contributes to its high performance in continuous flow systems.

To validate the practical application potential of the catalyst, we further investigated the catalytic performance of β-FeOOH@CF in river water reaction media to simulate real-world scenarios (Fig. 5(b)). Results demonstrate that β-FeOOH@CF exhibits outstanding catalytic activity, achieving complete conversion of 4-nitrophenol within 58 s in river water systems. This finding holds significant practical implications, providing potential technological support for water purification and environmental pollutant risk management.

Furthermore, β-FeOOH@CF maintained stable catalytic activity without regeneration during 10 consecutive cycles, achieving a catalytic reduction efficiency of 98.2% for 4-NP (Fig. 5(c)). The morphology (Fig. S13), XRD (Fig. S14a) and Raman patterns (Fig. S14b) of used β-FeOOH@CF showed no significant changes compared to the pristine sample, indicating excellent structural stability and reusability. The significant enhancement in catalytic activity of β-FeOOH@CF is attributed to the successful construction of its hierarchical composite structure, where β-FeOOH grows on a larger surface area, thereby improving reaction efficiency with 4-NP. These results demonstrate that β-FeOOH@CF exhibits versatile and promising catalytic activity for the reduction of nitrogen-containing organic pollutants. The high processing rate and outstanding durability of this catalytic fixed-bed system render it suitable for automated industrial production, delivering continuous, scalable, and sustainable performance.

3.3 Possible mechanistic understanding for the conversion of 4-nitrophenol to 4-aminophenol

To determine the acid–base environment of the reaction system, the pH of the solution at key steps was measured using a precision pH meter. The pH of the pure 4-nitrophenol aqueous solution was found to be 7.4. Upon addition of an excess of the reducing agent sodium borohydride ($NaBH_4$), the

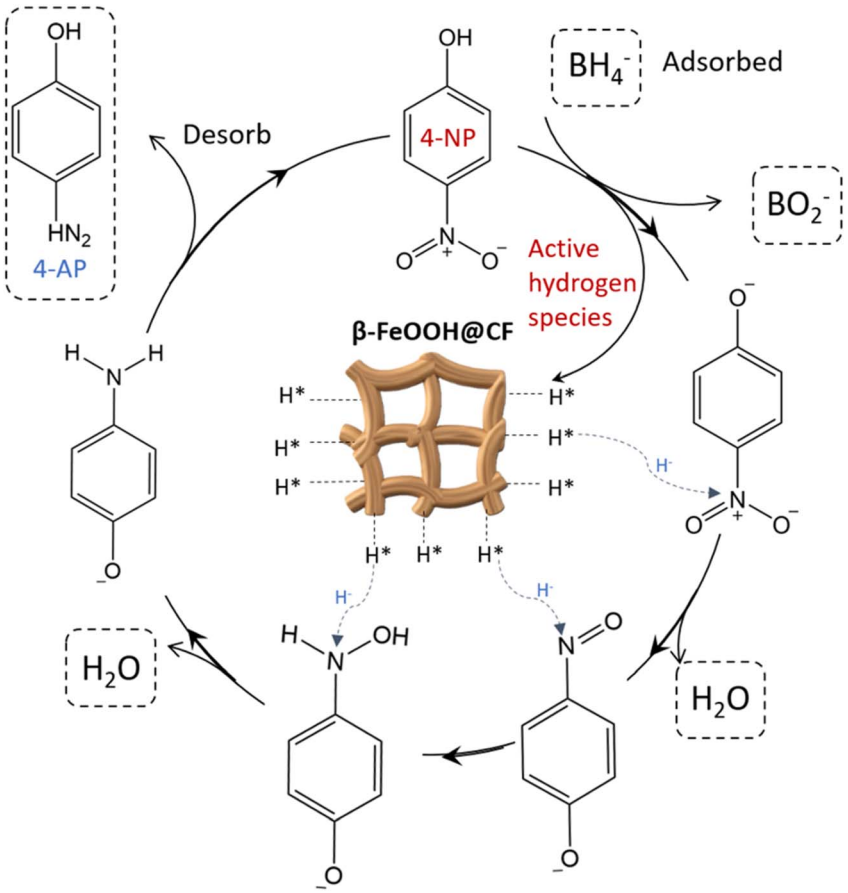

Fig. 6 Proposed mechanism for the reduction of 4-NP by the $NaBH_4$ with β-FeOOH@CF catalyst.

pH of the mixed solution rose to 9.3, indicating that the reaction proceeds under alkaline conditions. Under reaction conditions at pH = 9.3, the catalyst surface exhibited a negative zeta potential (Fig. S15), indicating a negatively charged state. At this pH, the reactant 4-nitrophenol also existed in anionic form, leading to electrostatic repulsion between the two species. This suggests the catalytic mechanism likely does not rely on strong adsorption of the reactant. Instead, it involves the efficient activation of the reducing agent sodium borohydride on the catalyst surface, generating abundant active hydrogen species, followed by hydrogen transfer and reduction reactions. These characterization results reveal the unique property of the catalyst to achieve efficient catalysis even under unfavorable electrostatic conditions.[58,59]

Following the Langmuir–Hinshelwood mechanism, a widely accepted model for evaluating catalytic efficiency, the catalytic mechanism of the β-FeOOH@CF catalyst for the reduction of 4-nitrophenol is elucidated.[60,61] Fig. 6 depicts the proposed mechanism for the reduction of 4-nitrophenol. In the aqueous system, BH_4^- ions generated by the ionization of sodium borohydride ($NaBH_4$) and 4-NP are respectively adsorbed on the catalyst surface. BH_4^- hydrolyzes to produce active hydrogen species (H*) under the catalysis of Fe^{3+}, during which Fe^{3+} is reduced to Fe^{2+};[62] however, copper foam (CF), with its excellent electrical conductivity, transfers electrons to Fe^{2+} to regenerate it into Fe^{3+}, forming a continuous Fe^{3+}/Fe^{2+} redox cycle.[63] To gain insight into the redox properties of the catalyst, cyclic voltammetry (CV) was performed on the β-FeOOH@CF catalyst in a 0.1 M Na_2SO_4 neutral electrolyte (Fig. S16). The results show a distinct oxidation peak was observed at +1.03 V (*vs.* Ag/AgCl), which is attributed to the oxidation of Fe^{2+} to Fe^{3+}. Subsequently, a reduction peak was detected at −0.94 V in the reverse scan. The well-defined redox peaks indicate a highly reversible Fe^{3+}/Fe^{2+} redox cycle.[64,65] To investigate the valence state changes and cycling of the active site Fe^{3+}/Fe^{2+} during the reaction, we performed XPS analysis on the post-reaction β-FeOOH@CF catalyst (Fig. S17). Analysis of the Fe 2p spectrum revealed a significantly enhanced signal intensity for Fe^{2+} (binding energy at ∼709.2 eV) compared to the fresh catalyst, indicating that part of the Fe^{3+} was reduced to Fe^{2+} during catalysis. Concurrently, the Fe^{3+} signal (∼711.0 eV) remained distinctly present, suggesting the occurrence of Fe^{2+} reoxidation back to Fe^{3+}. Subsequently, the adsorbed 4-NP undergoes stepwise hydrogenation *via* the intermediate 4-hydroxyaminophenol to form 4-aminophenol (4-AP). Due to its weaker adsorption affinity on the catalyst surface, 4-AP readily desorbs from the active sites. Throughout the process, the hierarchical pore structure of β-FeOOH@CF continuously facilitates mass transfer.[66] Ultimately, high-efficiency catalysis is achieved relying on the comprehensive effects of "mass transfer

enhancement, active site supply, redox cycle maintenance, and synergistic anti-agglomeration".

4. Conclusion

This study addresses the bottlenecks of low activity and high flow resistance in conventional packed-bed catalysts for the catalytic reduction of nitrogen-containing pollutants in continuous flow systems. The core innovation lies in the hydrothermal self-assembly of nano-flower-like β-FeOOH onto copper foam (CF), creating a monolithic β-FeOOH@CF catalyst tailored for continuous-flow fixed beds. This overcomes the limitations of traditional granular/powder catalysts in continuous-flow applications, which suffer from complex separation and agglomeration-induced high flow resistance. Under continuous-flow operation, this catalyst demonstrates outstanding performance: complete reduction of 4-nitrophenol (4-NP) within 49 seconds, with catalytic efficiency exceeding 98.2% even after 10 consecutive cycles. It also broadly degrades 2-NP, 3-NP and dyes like MO and CR while maintaining high activity in river water matrices. Its 3D hierarchical pore structure eliminates continuous flow mass transfer limitations, while CF conductivity sustains Fe^{3+}/Fe^{2+} redox cycling to ensure continuous catalytic kinetics-key adaptations for continuous flow systems. This study provides a novel strategy for designing continuous-flow environmental catalysts, advancing continuous-flow technology as a scalable, efficient solution for nitrogen-containing wastewater treatment. The continuous-flow system based on this catalyst holds significant industrial potential for automated water purification.

Conflicts of interest

The authors declare that there is no conflicts of interest.

Data availability

The data that support the findings of this study are available on request from the corresponding author. The data are not publicly available due to privacy or ethical restrictions.

Supplementary information (SI): the XRD, SEM, XPS, UV-Vis, Zeta potential, and cyclic voltammetry reulsts. See DOI: https://doi.org/10.1039/d5ra09414c.

Acknowledgements

This work was funded by the National Natural Science Foundation of China (Grant No. 22179038), the high score discipline construction project of Anhui Province (Project No. 061920), and the Young People Fund of Shandong First Medical University (202201-037).

References

1 N. J. Mondal, R. Sonkar, S. Thakur, N. C. Adhikary and D. Chowdhury, *ACS Appl. Nano Mater.*, 2023, **6**, 7351–7363.
2 S. Patar, S. Konwer, T. Chetia, B. K. Bhuyan and L. J. Borthakur, *ACS Appl. Nano Mater.*, 2023, **6**, 6567–6580.
3 M. Naushad, T. Ahamad and M. R. Khan, *Chemosphere*, 2022, **303**, 135173.
4 M. I. Din, R. Khalid, Z. Hussain, J. Najeeb, A. Sahrif, A. Intisar and E. Ahmed, *RSC Adv.*, 2020, **10**, 19041–19058.
5 R. Li, B. Wang, Y. Zhao, N. Zhang, X. Zhao, Z. Gao, H. Guo and H. Wang, *J. Environ. Chem. Eng.*, 2025, **13**, 118926.
6 Z. Chen, J. Li, J. Zhang, H. Wang, Y. Zeng, F. Wang, P. Huang, X. Chen, L. Ge, R. A. Dahlgren, H. Gao and X. Huang, *J. Clean. Prod.*, 2024, **435**, 140497.
7 Y. Lu, Y. Zhao, S. Wang and B. Hu, *Desalination*, 2026, **619**, 119488.
8 F. Jiang, Y. Zhang, X. Xu, Y. Mao, M. Wang, B. Yang, C. Zhang, X. Feng, H. Meng, F. Guo, Q. Han and S. Zhang, *J. Environ. Chem. Eng.*, 2025, **13**, 117556.
9 X. Li, Z. Wang, Y. Zhang, W. Zhang, H. Zhang, P. Liu and T. Lei, *J. Environ. Manage.*, 2025, **389**, 126016.
10 S. R. Manippady, A. Singh, B. M. Basavaraja, A. K. Samal, S. Srivastava and M. Saxena, *ACS Appl. Nano Mater.*, 2020, **3**, 1571–1582.
11 R. Li, X. Tang, J. Wu, K. Zhang, Q. Zhang, J. Wang, J. Zheng, S. Zheng, J. Fan, W. Zhang, X. Li and S. Cai, *Chem.–Eng. J.*, 2023, **464**, 142706.
12 R. Das, V. S. Sypu, H. K. Paumo, M. Bhaumik, V. Maharaj and A. Maity, *Appl. Catal., B*, 2019, **244**, 546–558.
13 Q. Zhang, R. J. Somerville, L. Chen, Y. Yu, Z. Fei, S. Wang, P. J. Dyson and D. Min, *J. Hazard. Mater.*, 2023, **443**, 130270.
14 P. Li, Y. Wang, H. Huang, S. Ma, H. Yang and Z.-L. Xu, *Chemosphere*, 2021, **263**, 127995.
15 C. Liu, Y.-L. Tong, X.-Q. Yu, H. Shen, Z. Zhu, Q. Li and S. Chen, *ACS Appl. Mater. Interfaces*, 2020, **12**, 2816–2825.
16 V. Kumar, I. Kaushal, A. K. Sharma, S. Sharma, A. Kumar, S. Bhukal, J. Rani and P. Saharan, *Appl. Surf. Sci.*, 2025, **688**, 162351.
17 J. Guo, Y. Gao, X. Cao, L. Li, X. Yu, S. Chi, H. Liu, G. Tian and X. Zhao, *Renew. Energy*, 2025, **244**, 122661.
18 L. Levin, M. Carabajal, M. Hofrichter and R. Ullrich, *Int. Biodeterior. Biodegrad.*, 2016, **107**, 174–179.
19 J. Min, B. Wang and X. Hu, *Sci. Rep.*, 2017, **7**, 5983.
20 S. F. M. Choobari, A. Nematollahzadeh and N. M. Babolan, *Chem. Eng. J.*, 2025, **510**, 161612.
21 M. Kohantorabi and M. R. Gholami, *Ind. Eng. Chem. Res.*, 2017, **56**, 1159–1167.
22 X. Sun, P. He, Z. Gao, Y. Liao, S. Weng, Z. Zhao, H. Song and Z. Zhao, *J. Colloid Interface Sci.*, 2019, **553**, 1–13.
23 F. M. Akwi and P. Watts, *Chem. Commun.*, 2018, **54**, 13894–13908.
24 J. He, W. Ji, L. Yao, Y. Wan, B. Khezr, R. D. Webster and H. Chen, *Adv. Mater.*, 2014, **26**, 4151–4155.
25 H. Hu, S. Du and J. Xi, *Green Chem.*, 2022, **24**, 5255–5264.
26 Z. Wang, K. Zhao, B. Xiao, P. Gao, D. He, T. Cai and J. Yuan, *Catalysts*, 2019, **9**, 981.
27 M. Shen, G. Zhao, Q. Nie, C. Meng, W. Sun, J. Si, Y. Liu and Y. Lu, *ACS Appl. Mater. Interfaces*, 2021, **13**, 28334–28347.
28 Q. Huang, P. Zhao, L. Lv, W. Zhang and B. Pan, *Environ. Sci. Technol.*, 2023, **57**, 9096–9104.

29 J. Harmel, L. Peres, M. Estrader, A. Berliet, S. Maury, A. Fécant, B. Chaudret, P. Serp and K. Soulantica, *Angew. Chem., Int. Ed.*, 2018, **57**, 10579–10583.
30 X. Sun, P. He, Z. Gao, Y. Liao, S. Weng, Z. Zhao, H. Song and Z. Zhao, *J. Mater. Chem. A*, 2024, **12**, 26038–26049.
31 A. Wu, X. Zhao, J. Wang, Z. Tang, T. Zhao, L. Niu, W. Yu, C. Yang, M. Fang, H. Lv, S. Liu and F. Wu, *Crit. Rev. Environ. Sci. Technol.*, 2021, **51**, 44–112.
32 F. Yu, C. Jia, X. Wu, L. Sun, Z. Shi, T. Teng, L. Lin, Z. He, J. Gao, S. Zhang, L. Wang, S. Wang and X. Zhu, *Nat. Commun.*, 2023, **14**, 4975.
33 Q. Yang, D. Chen, L. Chu and J. Wang, *J. Hazard. Mater.*, 2020, **389**, 122148.
34 K. Shanmugaraj, R. V. Mangalaraja, V. Manikandan, C. H. Campos, S. Packiaraj, R. Aepuru, J. N. Díaz de León, M. Sathish and K. S. Song, *J. Environ. Chem. Eng.*, 2024, **12**, 112942.
35 P. Zhao, B. Jin, Q. Zhang and R. Peng, *Appl. Surf. Sci.*, 2022, **586**, 152792.
36 M. Chen, Y. Zhang, J. Chen, R. Wang, B. Zhang, B. Song and P. Xu, *Small*, 2024, **20**, 2309371.
37 Z. Zhou, X. Li, Q. Li, Y. Zhao and H. Pang, *Mater. Today Chem.*, 2019, **11**, 169–196.
38 J. Du, Z. Chen, S. Ye, B. J. Wiley and T. J. Meyer, *Angew. Chem., Int. Ed.*, 2015, **54**, 2073–2078.
39 Y. Di, R. Zhao, J. Xiang, X. Meng, F. Wu and J. Li, *RSC Adv.*, 2023, **13**, 28713–28728.
40 J. J. De Yoreo, P. U. P. A. Gilbert, N. A. J. M. Sommerdijk, R. L. Penn, S. Whitelam, D. Joester, H. Zhang, J. D. Rimer, A. Navrotsky, J. F. Banfield, A. F. Wallace, F. M. Michel, F. C. Meldrum, H. Cölfen and P. M. Dove, *Science*, 2015, **349**, aaa6760.
41 L. Yu, R. Han, X. Sang, J. Liu, M. P. Thomas, B. M. Hudak, A. Patel, K. Page and B. S. Guiton, *ACS Nano*, 2018, **12**, 9051–9059.
42 X. Zhu, Z. Liu, H. Wang, R. Zhao, H. Chen, T. Wang, F. Wang, Y. Luo, Y. Wu and X. Sun, *Chem. Commun.*, 2019, **55**, 3987–3990.
43 M. K. Cho, J. H. Jo, J. U. Choi, J. Kim, H. Yashiro, S. Yuan, L. Shi, Y.-K. Sun and S.-T. Myung, *Nano Energy*, 2017, **41**, 687–696.
44 Y. Hu, J. Zhou, L. Li, Z. Hu, T. Yuan, C. Jing, R. Liu, S. Xi, H. Jiang, J.-Q. Wang and L. Zhang, *J. Mater. Chem. A*, 2022, **10**, 602–610.
45 T. Xi, C. Li, Y. Yu, W. Wei, S. Wang, T. Xu, H. Xiao, H. Dai, X. Zhou and H. Bian, *Adv. Compos. Hybrid. Mater.*, 2025, **8**, 196.
46 S. F. N. I., H. S. Chen, A. Anbalagan, Y. J. Huang, S. C. Haw, J. M. Chen, C. H. Lee, Y. H. Su and J. M. Ting, *Chem.–Eng. J.*, 2022, **438**, 135515.
47 X. Zhang, J. Ge, B. Lei, Y. Xue and Y. Du, *CrystEngComm*, 2015, **17**, 4064–4069.
48 F. Chen, C. Chen, Q. Hu, B. Xiang, T. Song, X. Zou, W. Li, B. Xiong and M. Deng, *Chem.–Eng. J.*, 2020, **401**, 126145.
49 S. Tai, J. Dhainaut, S. Royer, R. Zhong, S. Chen and N. Hammi, *Mater. Today Chem.*, 2025, **45**, 102692.
50 Z.-Y. Bi, S. Li, J.-H. Dai, L. Yang, P. Liu, J.-B. Xi and X. Peng, *Rare Met.*, 2025, **44**, 4679–4690.
51 M. Sultan, A. Javeed, M. Uroos, M. Imran, F. Jubeen, S. Nouren, N. Saleem, I. Bibi, R. Masood and W. Ahmed, *J. Hazard. Mater.*, 2018, **344**, 210–219.
52 K. Naseem, Z. H. Farooqi, R. Begum and A. Irfan, *J. Clean. Prod.*, 2018, **187**, 296–307.
53 R. Rajasekar, R. Thanasamy, M. Samuel, T. N. J. I. Edison and N. Raman, *Biochem. Eng. J.*, 2022, **187**, 108447.
54 G. Sharma, D. D. Dionysiou, S. Sharma, A. Kumar, A. H. Al-Muhtaseb, M. Naushad and F. J. Stadler, *Catal. Today*, 2019, **335**, 437–451.
55 C. Shang, B. Lu, C. Wu, S. Zhou, L. Shi, T. T. Isimjan and X. Yang, *Chin. Chem. Lett.*, 2025, **36**, 111152.
56 S. Lu, Y. Xue, F. Meng, M. Liu, T. Hou, Y. Luo, L. Liu, Y. An, G. Kang and X. Wu, *Carbon Capture Sci. Technol.*, 2025, **15**, 100433.
57 J. Wang, J. Zhang, G. Cheng, K. Zhang and X. Liu, *Environ. Technol. Innovation*, 2025, **39**, 104302.
58 S. Chen, L. Fang, Q. Zhu, L. Li and Z. Xing, *RSC Adv.*, 2016, **6**, 28257.
59 Z. Xiong, Z. Yi, M. Sakil, L. Huang, Z. Wang, X. Wu, Q. Wang, Z. Wang, G. Zhang, W. Zhang, S. Zhao and L. Zhu, *Sep. Purif. Technol.*, 2025, **356**, 129816.
60 P. P. P. Locatelli, M. Gurtat, G. F. Lenz, J. F. R. Marroquin, J. F. Felix, R. Schneider and C. E. Borba, *J. Hazard. Mater.*, 2021, **416**, 125801.
61 Y. M. Hunge, A. A. Yadav, S.-W. Kang, H. Kim, A. Fujishima and C. Terashima, *J. Hazard. Mater.*, 2021, **419**, 126453.
62 L. L. Cheng, Z. Y. Lu, J. J. Liu, J. Y. Liu, Y. Zhao, Z. B. Ni, Q. Q. Lin, R. L. Zhu, X. J. Chen, W. K. Lin, R. L. Qiu and Y. Zhu, *J. Mater. Chem. A*, 2024, **12**, 7890–7902.
63 H. H. Cao, Z. H. He, Y. Tian, Y. X. Yang, X. Wang, K. Wang, W. T. Wang, H. Wang, J. J. Liu and Z. T. Liu, *Appl. Catal., B*, 2025, **353**, 122689.
64 M. Wang, M. Liu, H. Zou and G. Liu, *Sep. Purif. Technol.*, 2025, **369**, 133067.
65 P. Wang, S. Gao, M. Geng and J. Tian, *Chem.–Eng. J.*, 2025, **513**, 162832.
66 Z. J. Zhu, Z. H. He, Y. Tian, S. W. Wang, Y. C. Sun, K. Wang, W. T. Wang, Z. F. Zhang, J. J. Liu and Z. T. Liu, *ACS Catal.*, 2025, **15**, 2145–2156.